Article

Current Biology

Orientation and direction tuning align with dendritic morphology and spatial connectivity in mouse visual cortex

Graphical abstract

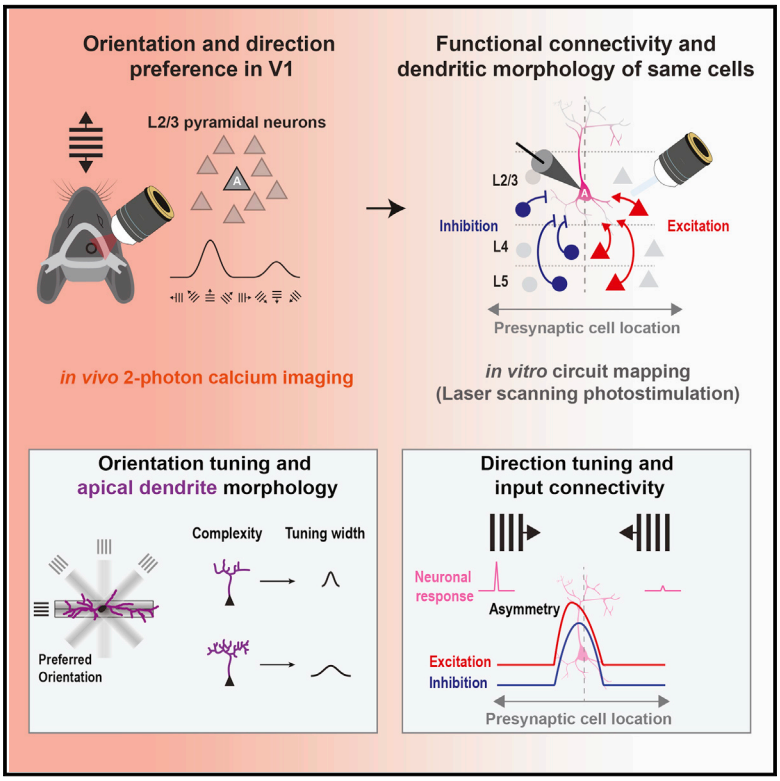

Highlights

- Functional *in vivo/in vitro* study of the same L2/3 pyramidal cells in mouse V1
- The apical dendrite is elongated along the postsynaptic preferred orientation
- The apical dendrite is less complex in sharply orientation-tuned cells
- Presynaptic neuron distribution is asymmetric along postsynaptic preferred direction

Authors

Simon Weiler, Drago Guggiana Nilo, Tobias Bonhoeffer, Mark Hübener, Tobias Rose, Volker Scheuss

Correspondence

volker.scheuss@med.uni-muenchen.de

In brief

Weiler et al. study the relationship between the visual tuning of L2/3 pyramidal cells, their dendritic morphology, and functional circuit connectivity. They show that orientation tuning is related to complexity and spatial elongation of the apical dendrite, and direction tuning aligns with asymmetries in the spatial organization of presynaptic neurons.

Weiler et al., 2022, Current Biology *32*, 1743–1753
April 25, 2022
https://doi.org/10.1016/j.cub.2022.02.048

CellPress

Current Biology

CellPress
OPEN ACCESS

Article

Orientation and direction tuning align with dendritic morphology and spatial connectivity in mouse visual cortex

Simon Weiler,[1,2,4,5] Drago Guggiana Nilo,[1,4,6] Tobias Bonhoeffer,[1,6] Mark Hübener,[1,6] Tobias Rose,[1,7] and Volker Scheuss[1,3,8,*]

[1]Max Planck Institute of Neurobiology, Martinsried, Germany
[2]Graduate School of Systemic Neurosciences, Ludwig-Maximilians-Universität München, Großhaderner Str. 2, 82152 Planegg, Germany
[3]Department of Psychiatry, Ludwig-Maximilians-Universität München, Nussbaumstr. 7, 80336 München, Germany
[4]These authors contributed equally
[5]Present address: Sainsbury Wellcome Centre for Neural Circuits and Behaviour, University College London, 25 Howland Street, London W1T 4JG, UK
[6]Present address: Max Planck Institute for Biological Intelligence, in foundation, Martinsried, Germany
[7]Present address: Institute for Experimental Epileptology and Cognition Research, University of Bonn, Venusberg, Campus 1, 53127 Bonn, Germany
[8]Lead contact
*Correspondence: volker.scheuss@med.uni-muenchen.de
https://doi.org/10.1016/j.cub.2022.02.048

SUMMARY

The functional properties of neocortical pyramidal cells (PCs), such as direction and orientation selectivity in visual cortex, predominantly derive from their excitatory and inhibitory inputs. For layer 2/3 (L2/3) PCs, the detailed relationship between their functional properties and how they sample and integrate information across cortical space is not fully understood. Here, we study this relationship by combining functional *in vivo* two-photon calcium imaging, *in vitro* functional circuit mapping, and dendritic reconstruction of the same L2/3 PCs in mouse visual cortex. Our work reveals direct correlations between dendritic morphology and functional input connectivity and the orientation as well as direction tuning of L2/3 PCs. First, the apical dendritic tree is elongated along the postsynaptic preferred orientation, considering the representation of visual space in the cortex as determined by its retinotopic organization. Additionally, sharply orientation-tuned cells show a less complex apical tree compared with broadly tuned cells. Second, in direction-selective L2/3 PCs, the spatial distribution of presynaptic partners is offset from the soma opposite to the preferred direction. Importantly, although the presynaptic excitatory and inhibitory input distributions spatially overlap on average, the excitatory input distribution is spatially skewed along the preferred direction, in contrast to the inhibitory distribution. Finally, the degree of asymmetry is positively correlated with the direction selectivity of the postsynaptic L2/3 PC. These results show that the dendritic architecture and the spatial arrangement of excitatory and inhibitory presynaptic cells of L2/3 PCs play important roles in shaping their orientation and direction tuning.

INTRODUCTION

The response properties of neurons derive to a large part from the integration of their synaptic inputs. Neurons in the mammalian visual system, such as layer 2/3 pyramidal cells (L2/3 PCs) in the visual cortex, integrate inputs with specific receptive fields in visual space. The biased sampling of visual space by receptive fields is the basis for a neuron's visual response properties, such as orientation and direction selectivity.[1–3] Crucially, visual space is represented systematically across the visual cortex, forming a retinotopic map.[4–6] Thus, how a neuron samples its cortical neighborhood will directly and predictably determine its visual response properties.

The first fundamental factor constraining how a neuron samples inputs from its neighborhood is its dendritic architecture.[7] The dendritic morphology of L2/3 PCs in primary visual cortex (V1) varies in terms of both complexity and spatial extent.[8] In principle, specialized dendritic architectures can give rise to biased sampling of inputs across the representation of visual space in V1, resulting in specific tuning properties. For example, it has been proposed that neurons in V1 are endowed with orientation or direction tuning by way of their elongated or asymmetric dendrites.[9,10] For basal dendrites, however, although pronounced asymmetries exist, it has been found that these asymmetries have no relation to either the orientation or direction preference of neurons in monkey and cat visual cortices.[11,12] However, whether this holds also in rodents—

which have a functional salt-and-pepper organization[13]—remains open. Apical dendrite inputs and dendritic processing have been shown to enhance orientation selectivity in L2/3 PCs,[14,15] suggesting a prominent role of the apical dendrite in tuning selectivity (but see Park et al.[16]). Whether apical dendritic architecture contributes to visual stimulus selectivity remains unknown.

In addition to dendritic morphology, a key determinant of how a neuron samples its cortical neighborhood and ultimately acquires its response properties is its embedding in functional microcircuits. The microcircuit is defined by intralaminar and interlaminar excitatory and inhibitory synaptic connections and their respective functional strengths (reviewed in Harris and Mrsic-Flogel[17]). Apart from connection probabilities and, on average, a spatial balance of the sources of excitation and inhibition across layers,[18–20] little is known about the functional microcircuit of L2/3 PCs in V1 and its role in visual tuning. Nevertheless, several observations point toward the microcircuit, displaying signatures of visual tuning inheritance and *de novo* generation: Higher functional connection strength and probability are found in pairs of L2/3 PCs when these display similar response properties.[20] Furthermore, spatial signatures of biased sampling in visual space have been observed for orientation and direction tuning. At the level of visual space, receptive fields of excitatory but not inhibitory presynaptic L2/3 neurons tend to be aligned to the axis of the postsynaptic L2/3 PC's preferred orientation.[21–23] L2/3 PC direction tuning, on the other hand, is associated with a spatiotemporal offset of excitation and inhibition.[10,23] However, such spatial relationships of receptive fields in visual space do not map one-to-one to the arrangement of the corresponding presynaptic neurons in cortex.[5,23] Furthermore, the cortical distribution of presynaptic neurons based on anatomical connectivity alone[23] does not provide information about the distribution of response strength over the receptive field.[24,25]

Here, we employ a combined *in vivo-in vitro* approach[26] to directly relate dendritic morphology and input connectivity to the orientation and direction tuning of L2/3 PCs. We first characterized the tuning properties of individual L2/3 PCs in mouse binocular primary visual cortex (bV1) using *in vivo* two-photon calcium imaging. We then reidentified the same L2/3 PCs in acute brain slices and mapped their monosynaptic intralaminar and interlaminar excitatory and inhibitory inputs using laser-scanning photostimulation (LSPS).[27,28] Additionally, we filled the cells with Alexa-594 and reconstructed their dendritic trees. This approach enabled us to directly compare tuning selectivity and tuning preference with functional connectivity in the same cells.

We find that the apical dendrites of orientation-selective L2/3 PCs are elongated along their preferred orientation considering retinotopy. Additionally, the complexity of apical dendrites is correlated with the sharpness of orientation tuning. In direction-selective L2/3 PCs, the excitatory but not the inhibitory input distribution displays a spatial asymmetry around its mean, and the degree of this asymmetry is correlated with the neuron's direction selectivity.

RESULTS

Assessing visual response properties and neuronal circuit connectivity of the same neurons

For studying the relationship between dendritic architecture, neuronal circuit connectivity, and sensory processing in mouse L2/3 PCs, we determined their visual response properties, intralaminar and interlaminar functional synaptic inputs, and neuronal morphology (Figure 1A). We recorded visually evoked activity of individual L2/3 PCs coexpressing GCaMP6m and mRuby2 in the binocular zone of primary visual cortex (bV1) using two-photon calcium imaging (Figures 1Bi and 1Bii). One day after functional imaging, we prepared coronal slices, identified the previously imaged PCs, and mapped their monosynaptic excitatory and inhibitory inputs by LSPS via UV-glutamate uncaging at different laminar and tangential locations.[26–28] This way, we were able to map the spatial distribution and strength of excitatory and inhibitory presynaptic partners for each PC across cortical layers (Figures 1Ci, 1Cii, and S1). Neurons were filled with Alexa-594, and their dendritic morphology was imaged by two-photon microscopy. In total, we characterized the visual tuning properties and local excitatory and inhibitory synaptic inputs of 70 L2/3 PCs. In 36 of these cells, the dendritic morphology was reconstructed (overview of all cells in Figure S1).

Apical dendritic morphology directly relates to orientation tuning of L2/3 pyramidal cells

The dendritic architecture of L2/3 PCs varies in complexity and spatial extent.[8] Since it determines the sampling of axons[7] and axonal projections are retinotopically organized (e.g., Marques et al.[29]), we reasoned that features of dendritic architecture might be reflected in the visual response properties of L2/3 PCs.

Comparison of the dendritic morphologies of L2/3 PCs and their tuning curves (examples of two cells at similar cortical depth in Figures 2A and 2B) suggested that apical tree morphology varies with orientation tuning. To quantify this relationship, we evaluated three parameters related to dendritic length and extent (total dendritic length, maximal horizontal extent, and distance to peak Sholl crossing; STAR Methods) as well as two parameters related to dendritic complexity (number of branch points and peak number of Sholl crossings; Figures 2F and S2) for both the apical and basal dendrites. The retinotopic organization of mouse V1[4] allowed us to estimate the spatial pattern of the activity evoked by the oriented stimulus bars in the coronal brain slice (see STAR Methods, Figure S3, and Waters et al.[30]). Accordingly, the activity evoked by a bar with an orientation of ~106° in visual space aligns along the coronal slice, whereas a bar with an orientation of ~53° evokes activity that is oriented perpendicular to the slice plane (Figure 2C). These directions in visual space, corresponding to the perpendicular cortical axes along and across the coronal slice, are not orthogonal as one might expect because the cortical magnification factor is not constant across visual space.[4] Strikingly, we observed a significant circular correlation (cc) between the preferred orientation and the maximal horizontal extent of the apical but not the basal dendritic tree of L2/3 PCs ($cc = 0.5$, $p < 0.023$, $cc = 0.19$, $p = 0.598$; Figures 2D and 2E). Considering retinotopy, the apical tree's horizontal extent along the slice is larger for cells with a preferred orientation around the particular orientation in visual

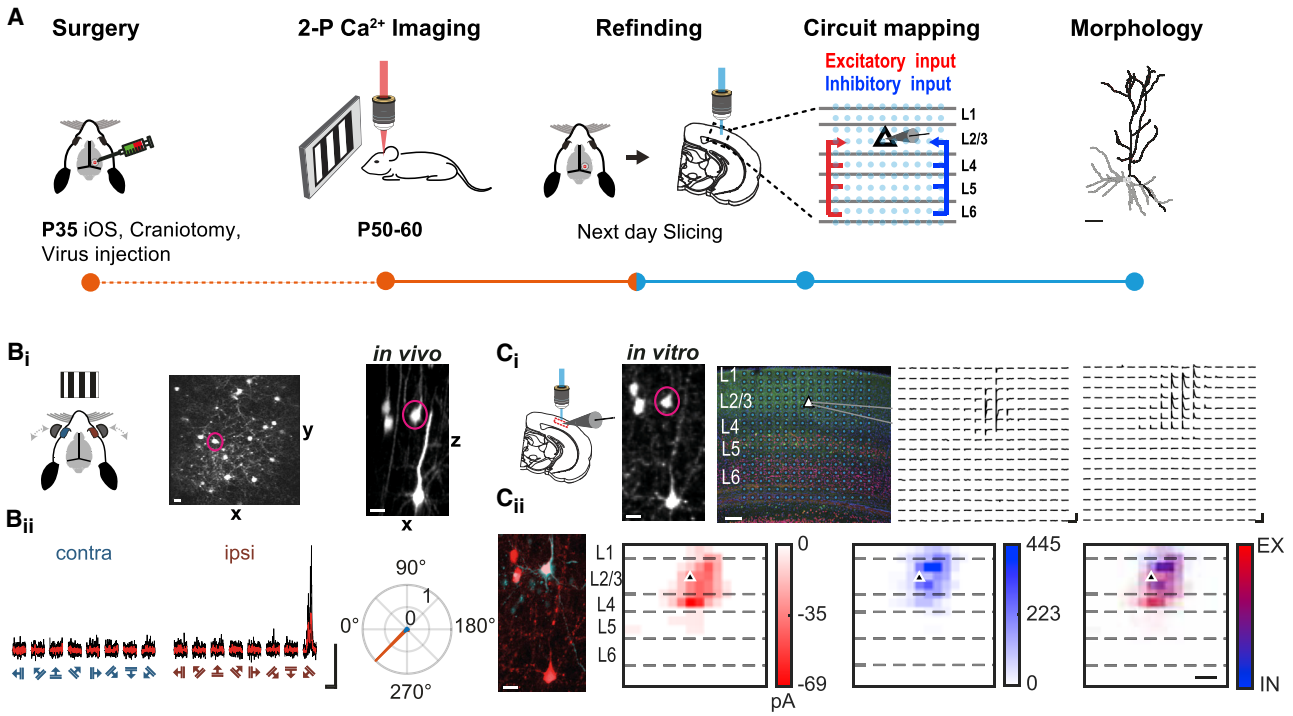

Figure 1. *In vivo-in vitro* approach measures visual response properties, morphology, and corresponding laminar and inhibitory inputs of L2/3 pyramidal cells in V1

(A) Experimental *in vivo-in vitro* pipeline: GCaMP6m and mRuby2 were expressed in bV1 and visual response properties of L2/3 PCs were characterized using *in vivo* two-photon calcium imaging. Subsequently, L2/3 PCs were refound in acute brain slices and the laminar excitatory and inhibitory inputs were mapped using LSPS by UV-glutamate uncaging. Additionally, L2/3 PCs were filled with Alexa-594 to reconstruct their dendritic morphology. Reconstructed L2/3 PC dendritic morphology is from cell shown in (B) and (C) (scale bars, 50 μm).

(B and C) Example of an *in vivo-in vitro* characterized cell (see also Figure S1).

(B_i) Visual stimulation paradigm (depicted in schematic). The L2/3 PC of interest is marked by a circle in the top and side views of the structural image stack obtained *in vivo* (top, maximum intensity projections; scale bars, 25 μm).

(B_{ii}) Calcium transients of the cell in response to ipsilateral or contralateral eye stimulations with drifting gratings of eight orientations. Individual calcium transients are shown in black; average in red (scale bars, $\Delta R/R_0$ = 200%, 10 s). Polar plot of peak-normalized directional responses to contralateral and ipsilateral eye stimulation (blue and red, respectively).

(C_i) Circuit mapping *in vitro*. The L2/3 PC depicted in (B) is marked by a circle in the *in vitro* side view (top, maximum intensity projection; scale bars, 25 μm). Stimulation grid (blue dots) overlaid on brain slice with schematic patch pipette on L2/3 PC. Histological labels mark neocortical layers: L2/3, calbindin (green); L5/6, CTIP2 (red). All cells stained with DAPI (blue; scale bars, 100 μm). Excitatory currents (cell clamped to −70 mV) and inhibitory currents (cell clamped to 0 mV; scale bars, 250 pA, 500 ms) evoked at corresponding stimulus grid locations.

(C_{ii}) The L2/3 PC depicted in (B) was filled with Alexa-594 (cyan). Reconstructed dendritic morphology is shown in (A). Pixel-based excitatory (red) and inhibitory (blue) input maps represented with color-coded response amplitudes and overlay of both (right; scale bars, 100 μm).

space that corresponds to the medial-lateral axis along the coronal slice in cortical space (here: ~106°; Figures 2C and S3). Under the assumption of overall morphological anisotropy in dendritic structure with respect to the anterior-posterior and medial-lateral cortical axes, this suggests that the apical tree preferentially samples synaptic inputs at cortical sites along the extent of a stimulus' representation—which corresponds to the cell's preferred orientation—as has been previously hypothesized.[9]

Moreover, when comparing the dendritic tree complexity (Figure 2F) and orientation tuning, we found a significant correlation between orientation tuning width and the peak number of Sholl crossings of the apical dendrite as well as its total number of branch points linking apical dendritic complexity with tuning width (Figures 2G, S2C, and S4; peak number of Sholl crossings, r = 0.58, p = 0.001; number of branch points, r = 0.36, p = 0.05). A similar relationship holds for the global orientation selectivity index (gOSI; STAR Methods; Figure S2C). In contrast, basal tree morphology did not show such correlations (Figures 2H and S2; r = 0.12, p = 0.522; r = 0.15, p = 0.418). None of the parameters for apical nor basal spatial extent or total length significantly correlated with orientation selectivity or tuning width (Figure S2C).

Figure 2A shows that L2/3 PCs at the same cortical depth can have very different morphologies. Considering that a cell's cortical depth influences its morphology by imposing limits on the vertical extent of the apical dendrite, the relationship between apical dendrite complexity and orientation selectivity might be linked to differences in cortical depth. However, orientation selectivity as well as tuning width did not show a significant correlation with cortical depth (r = 0.07, p = 0.716; r = −0.33, p = 0.074; Figure S2E). Moreover, although the number of branch

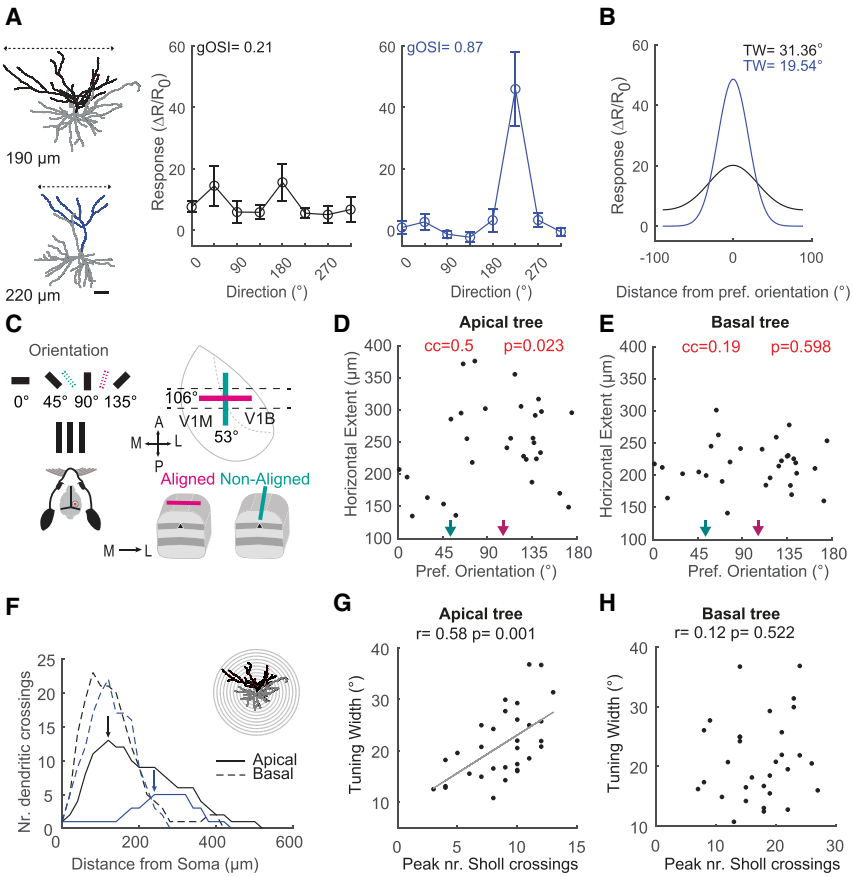

Figure 2. Apical but not basal dendritic morphology is related to orientation preference and tuning sharpness

(A) Representative basal (gray) and apical dendritic morphologies (black/blue) of two L2/3 PCs with low (top left) and high orientation selectivities (bottom left; pial depths are indicated). The maximum horizontal extent for the apical dendrites of both cells is indicated with dashed lines. Tuning curves and global orientation selectivity index (gOSI) for the two depicted cells (mean ± SEM, n = 4 repetitions; scale bars, 50 µm; see also Figure S2).

(B) Double Gaussian fit of the tuning curves (STAR Methods) shown over the interval around the preferred orientation for the cells in (A). Tuning width (TW) listed on the right.

(C) Schematic displaying the gratings presented to the mouse at different orientations (left) and the representation of the evoked activity by the stimulus grating in cortical space (top right). Dashed lines indicate the coronal brain slice orientation used for circuit mapping (V1M, monocular V1; V1B, binocular V1; M, medial; L, lateral; P, posterior, A, anterior). Representation of the stimulus orientation along the coronal brain slice (aligned) and orthogonal to the brain slice (nonaligned; bottom right). For visual to cortical space mapping, see also Figure S3.

(D) Orientation preference plotted against horizontal extent of the apical tree (n = 30 cells). Circular correlation is indicated. Arrows indicate the representation of the stimulus orientations in visual space for aligned and nonaligned cells.

(E) Same as (D) for the basal trees.

(F) Sholl analysis for apical and basal dendritic trees for the two cells shown in (A). Arrows indicate the peak number of crossings of the apical trees (see also Figure S2).

(G) Tuning width plotted against the peak number of Sholl crossings (n = 31 cells). Linear fit and Pearson correlation value indicated (see also Figure S4).

(H) Same as (G) for the basal trees.

points of the apical tree did not show a significant correlation with cortical depth ($r = -0.01$, $p = 0.957$), there was a small but significant correlation between peak number of Sholl crossings and pial depth ($r = -0.38$, $p = 0.035$; Figure S2F). This indicates that the differences in apical dendrite complexity between highly orientation-selective and more broadly tuned neurons are unlikely due to differences in laminar position.

Taken together, we find that the apical dendritic architecture directly relates to the orientation tuning of L2/3 PCs in visual cortex. However, we did not find such a relation with orientation tuning for the basal dendritic architecture.

Cortical microcircuits underlying visual response properties

Although the dendritic architecture indirectly represents the sampling of cortical and thereby visual space, we also directly probed the spatial arrangement of local presynaptic partners of L2/3 PCs.

We found that the laminar and horizontal distributions of inputs to L2/3 PCs in bV1 were diverse (Figures 3A and S1). To quantify this diversity, we peak normalized the input maps and computed the input fractions per row and column of the stimulation grid. We excluded any excitatory input from L1 since this layer does not contain excitatory neurons, and the observed input in L1 originates most likely from activated excitatory cells located at the border between L2/3 and L1 or apical tufts of L4 PCs[18,28] (STAR Methods; Figures S5A–S5C). Most excitatory as well as inhibitory input arose from L2/3, less from L4, little from L5, and some inhibition from L1 (Figure 3B). Since we recorded excitatory and inhibitory inputs in the same cells, we were able to assess the spatial E/I relationship on a cell-to-cell basis. Noteworthy, the layer-by-layer excitatory and inhibitory inputs were balanced only for a minority of cells. There was a wide distribution of the relative amounts of excitation and inhibition at the single-cell level, with a significant number of cells receiving stronger inhibition than excitation from within L2/3 (Figures 3B and S5D; Wilcoxon signed-rank, $p < 0.001$). In contrast, most cells received stronger excitation than inhibition from both L4 and L5 (Figures 3B and S5D; Wilcoxon signed-rank, $p < 0.001$).

Horizontally, the spatial distribution of the excitatory and inhibitory presynaptic partners was on average centered on the soma across L2/3, L4, and L5 (Figure 3C). Notably, while inhibitory presynaptic sources were more concentrated

CellPress
OPEN ACCESS

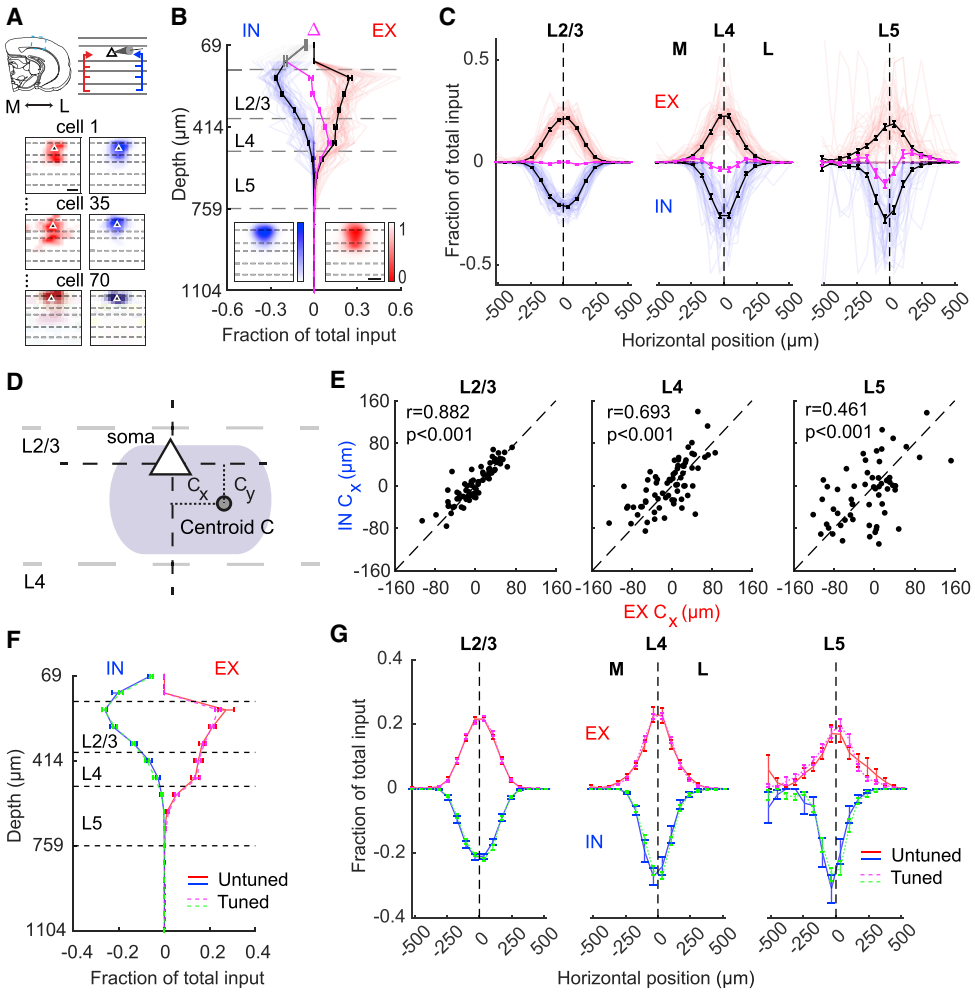

Figure 3. Laminar and horizontal distributions of local excitatory and inhibitory inputs to functionally characterized cells are diverse

(A) Alignment of input maps along the medial-lateral axis preceding analysis. Representative peak-normalized excitatory and inhibitory inputs maps for three cells (scale bars, 100 μm).

(B) Average vertical excitatory (EX, red) and inhibitory (IN, blue) input fractions per stimulus row; thin lines, individual cells. The average difference between vertical excitatory and inhibitory input fractions is shown in magenta (mean ± SEM, n = 70 cells). Insets depict averaged normalized maps of all cells. Light gray areas in L1 not considered for comparison (see also Figure S5).

(C) Same as in (B), for horizontal excitatory and inhibitory input fraction per column for L2/3, L4, and L5.

(D) Schematic depicting the position of the centroid C of an input map within L2/3 relative to the cell soma. The horizontal and vertical offsets between soma and centroid were determined (C_x and C_y).

(E) C_x of inhibition plotted against C_x of excitation in L2/3, L4, and L5. Unity lines are indicated. Pearson correlation coefficient r indicated at top of each plot.

(F) Average vertical excitatory (EX) and inhibitory (IN) input fractions per stimulus row for orientation-tuned (mean ± SEM, n = 50 cells) and untuned L2/3 PCs (mean ± SEM, n = 20 cells).

(G) Same as in (F) for horizontal excitatory and inhibitory input fractions per column for L2/3, L4, and L5.

around the postsynaptic soma (putatively representing perisomatic inhibition[31]), excitatory presynaptic sources dominated slightly more distal regions, resulting in an "inverted Mexican hat" profile[23,32] (Figure 3C). This was most prominent in L4 and L5 (Figure 3C, middle and right, and Figure S5E; Wilcoxon signed-rank, $p < 0.001$) and not detectable in L2/3 (Figure 3C, left, and Figure S5E; Wilcoxon signed-rank, $p = 0.169$).

To explore the spatial structure of the input maps in more detail, we calculated the position of their weighted centroids (arithmetic mean of the locations of the points in the input map, weighted by their input amplitude). This allowed us to quantify the horizontal and vertical offsets of the presynaptic cell distributions in the different layers relative to the postsynaptic soma (C_x and C_y, Figure 3D) that may represent biases in input sampling. On average, the centroids of excitatory and inhibitory inputs coincided in their position along the horizontal axis within all layers (Figure 3E). In particular, in L2/3, this correlation was very strong.

In conclusion, although on average, excitation and inhibition follow each other spatially across layers, we find that individual L2/3 PCs varied in their input map organization.

Laminar excitatory and inhibitory input distributions are unrelated to orientation selectivity

Given the observed variations in the input maps of individual L2/3 PCs, we wondered how these relate to their visual response properties. To compare the spatial organization of excitatory and inhibitory presynaptic partners of orientation-selective and nonselective L2/3 PCs, we categorized them into orientation-tuned (gOSI > 0.25) and orientation-untuned cells (gOSI ≤ 0.25 or unresponsive to gratings; STAR Methods). We did not find statistically significant differences in either the laminar or the horizontal input distributions between these two groups (Figures 3F and 3G; Wilcoxon rank-sum, all laminar comparisons were $p > 0.13$, all horizontal comparisons were $p > 0.065$, only columns with at least three data points were considered). Similarly, there was no statistically significant difference between these two groups when comparing the differences between the excitatory and inhibitory laminar as well as horizontal input fractions (e.g., inverted Mexican hat profile; data not shown).

Directional spatial presynaptic connectivity and direction tuning of L2/3 PCs

Spatial asymmetry between excitation and inhibition has been proposed to play a role in cortical direction tuning.[10,23] Thus, we analyzed the spatial organization of functional excitatory and inhibitory inputs of individual L2/3 PCs with respect to their direction tuning. In a coronal slice, an input map represents a section of the three-dimensional distribution of the presynaptic neurons of a given L2/3 PC at a particular angle. This angle can be related to the preferred direction of the L2/3 PC mapped onto cortical space, similarly to the alignment of preferred orientation described above (Figure 2C). Accordingly, a bar moving in the directions of ∼106° or ∼286° would evoke activity progressing along the slice (aligned), whereas a bar moving in the directions of ∼53° or ∼233° would evoke activity running orthogonally to the slice plane (nonaligned, Figure 4A; see also STAR Methods and Figure S3).

To probe the relation between direction preference and the spatial organization of input maps, we computed a rolling average of the weighted centroid C_x across the preferred direction for both excitation and inhibition from within L2/3 (Figure 4B). This rolling average displayed a minimum and maximum close to the "along-slice" directions of 106° and 286°. We then pooled the input maps for cells that had preferred directions of ∼106° and ∼286° by mapping both to the same direction and compared them with the combined maps for nonaligned orthogonal directions (∼53° and ∼233°, averaged over an 80° sector; STAR Methods). In L2/3 PCs with aligned preferred directions, the horizontal centroid position for intralaminar input had a significant negative offset compared with cells preferring the nonaligned directions, both for excitation and inhibition (Figure 4C; Wilcoxon rank-sum, $p < 0.001$). Spatial offsets were also present for presynaptic input distributions within L4 and L5, but only the input from L4 showed significant negative offsets for cells with aligned versus nonaligned preferred direction, like the input from L2/3 (Figure S5F; Wilcoxon rank-sum, $p = 0.018$ for excitation, $p = 0.025$ for inhibition). In the cells with aligned preferred direction, the centroid locations of the excitatory and inhibitory presynaptic cell distributions were not significantly different, arguing against a substantial offset between excitation and inhibition (Figure S5G; Wilcoxon signed-rank; L2/3, $p = 0.945$; L4, $p = 0.844$; L5, $p = 0.813$).

We also noted that the excitatory presynaptic input distribution was spatially skewed when comparing the average and the individual horizontal input profiles for cells with aligned and nonaligned preferred directions (Figure 4D). In cells with aligned preferred direction, the input profile's shoulders were steep on the side opposite—and long on the side along—the preferred direction. To quantify this skew, we analyzed the slope of the spatial input distribution profiles on both sides toward the preferred and the null direction (STAR Methods). Although the difference in length of rise between the preferred and null sides was not significant for either excitation or inhibition in both groups (Figures 4E and 4F; AL versus NAL; EX, $p = 0.313$; IN, $p = 0.547$), we found that the rise of excitation in the aligned cells with higher direction selectivity was steeper toward the preferred than to the null direction (coloring in Figure 4E, top).

To quantify this relationship, we tested whether the degree of the observed asymmetry in excitation (Figure 4E, top) was correlated with the direction selectivity of L2/3 PCs. Indeed, the ratio of the spatial rates of rise (toward preferred over toward null direction) of the excitatory input distribution showed a strong positive correlation with the degree of direction selectivity of the postsynaptic L2/3 PC (Figure 4G; $r = 0.82$, $p = 0.013$). This relation was not present for the inhibitory input distribution (Figure 4G; $r = -0.22$, $p = 0.605$).

In conclusion, we find that the presynaptic cells of a direction-tuned L2/3 PC tile its neighborhood in a biased way. We observe an asymmetry in the distribution of presynaptic partners along the cell's preferred direction, where the degree of this spatial asymmetry correlated with the degree of its direction selectivity.

DISCUSSION

We investigated the relationship between cellular morphology, input connectivity, and tuning for orientation and direction in individual L2/3 PCs in mouse bV1 and found that the dendritic architecture of L2/3 PCs displayed a clear correlation with their respective orientation tuning. The apical but not the basal dendritic tree was elongated along the postsynaptic preferred orientation in relation to the representation of visual space in the cortex. Sharply orientation-tuned cells had less complex apical dendrites than broadly tuned cells. Furthermore, we found spatial offsets in the distributions of excitatory and inhibitory presynaptic neurons with respect to the soma of L2/3 PCs. These offsets were opposite to the preferred direction in direction-tuned L2/3 PCs. Finally, the presynaptic excitatory but not inhibitory input distributions displayed asymmetries that were correlated with the postsynaptic direction selectivity.

Orientation selectivity and dendritic structure

Although subtypes of neurons in visual cortex have been reported to differ in both their morphology and visual response properties,[33,34] detailed analysis of, for example, basal dendrite asymmetries has revealed no relation to orientation or direction selectivity.[11,12,35] Here, we found what is to our knowledge the first evidence for interdependence between cellular morphology and orientation tuning in the visual cortex: The apical tree was

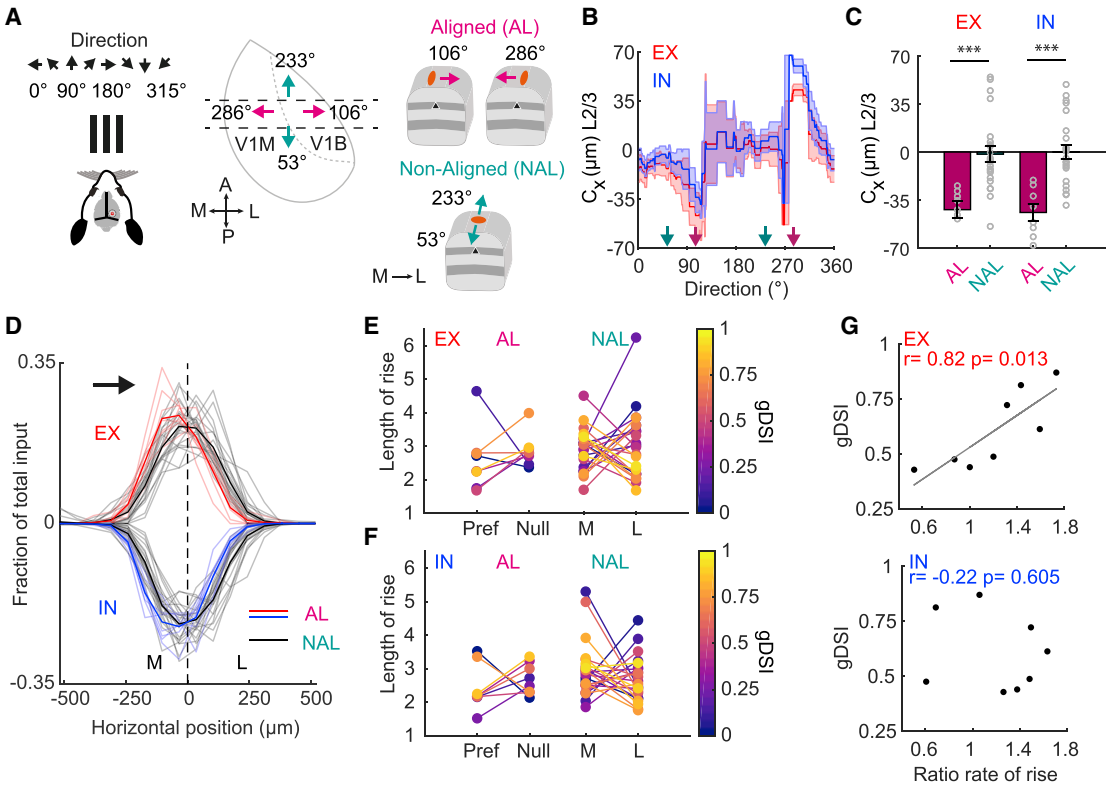

Figure 4. Asymmetry of input distributions correlates with direction tuning

(A) Schematic displaying gratings presented to the mouse at different directions (left) and the representation of stimulus motion in cortical space (middle). Dashed lines indicate the coronal brain slices (V1M, monocular V1; V1B, binocular V1; M, medial; L, lateral; P, posterior; A, anterior). Schematic depicting the representation of the directions of a moving bar along the coronal brain slice (aligned) and orthogonal to the brain slice (nonaligned). Arrows indicate directions of the moving bars. Triangle indicates postsynaptic L2/3 PC (right). For estimates, see Figure S3.

(B) Rolling average of excitatory (red) and inhibitory (blue) C_x in L2/3 across direction preference using a window size of 65°. SEM is indicated as the shaded area. Only cells with gDSI > 0.25 are included (n = 38 cells).

(C) Comparison of the average C_x in L2/3 for cells with preferred direction ~106°/~286° (AL) and ~53°/~233° (NAL) for excitation (left) and inhibition (right). Mapping data for 286° onto data for 106° (AL) and data for 233° onto data for 53° (NAL) the sign of the respective C_x was inverted. Individual data points are superimposed (mean ± SEM; AL, n = 8 cells; NAL, n = 20 cells). One-tailed Wilcoxon rank-sum test (see also Figure S5).

(D) Individual and average excitatory and inhibitory horizontal input fraction per column for L2/3 for cells with preferred direction ~106°/~286° (AL, blue and red lines) and ~53°/~233° (NAL, black lines). Arrow indicates preferred direction.

(E) Length of spatial rise of excitatory (top) and inhibitory (bottom) input distribution at preferred and null directions (units spacing of stimulus grid, aligned cells, n = 8 cells). Color code depicts the gDSI.

(F) Same as (E) for nonaligned cells (n = 20 cells).

(G) gDSI plotted against ratio rate of rise between the preferred and the null direction for excitation (top) and inhibition (bottom). Linear fit for excitation and Pearson correlation values indicated.

elongated along the L2/3 PC's preferred orientation considering retinotopy. This could, in principle, allow biased synaptic input sampling from the cortical neighborhood in a way supporting orientation selectivity by biased sampling of visual space, as previously hypothesized[9] (Figure 5A). In addition, sharply orientation-tuned L2/3 PCs had a less complex apical dendritic tree compared with broadly tuned cells. A more complex apical dendrite could, in principle, allow denser sampling from nearby axons,[7] permitting integration of a more diverse range of inputs and leading to broader somatic tuning. The basal dendritic tree did not show such relationships to orientation tuning as in cats and monkeys.[11,12,35]

The observed differences between apical and basal dendrite in the context of orientation tuning might arise from different input sampling strategies and/or differential roles of these cellular compartments in the generation of the postsynaptic visual response properties.[29,37] Apical dendrites of L2/3 PCs may receive inputs that display both lower (thalamic nuclei[38,39]) and higher orientation selectivities (direction-selective retinal ganglion cells via LGN, cortico-cortical feedback[40–42]) than the cell's output itself. In contrast, basal dendrites receive primarily feedforward input from L4 and L2/3,[43,44] both of which display similar orientation selectivity.[45] Since it was shown that ablation of neither apical nor basal dendrites by microdissection strongly alters orientation tuning of L2/3 PCs,[16] the difference in how apical and basal dendrite morphologies are related to orientation tuning might reflect the different ways of integrating their distinct inputs for arriving at similar overall orientation selectivity.

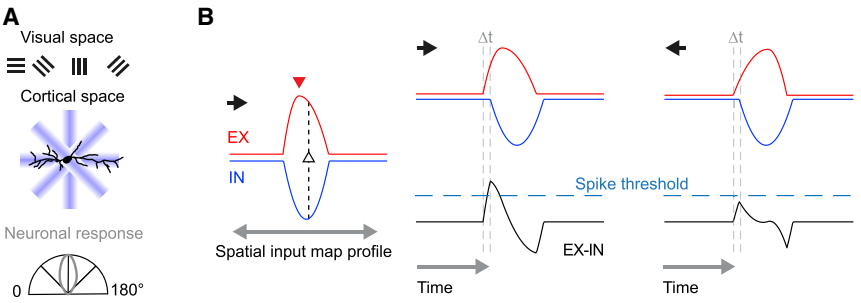

Figure 5. Schematic illustrating how the observed asymmetries in dendritic morphology and spatial input distribution could contribute to cortical orientation and direction tuning

(A) Dendritic morphology and orientation tuning: based on retinotopy, grating stimuli presented to the mouse at different orientations in visual space (top) are associated with specific axes in cortical space (view from pia down onto cell). An orientation-selective L2/3 PC (polar plot, bottom) displays an elongation in its apical dendrite. The axis of this elongation in cortical space corresponds to the cell's preferred orientation in visual space. Thus, dendritic elongation can contribute to spatially biased cortical connectivity underlying the reported alignment of the receptive fields of presynaptic partners that is co-oriented to the preferred orientation of orientation-selective L2/3 PCs.[9,21–23,36]

(B) Spatial input distribution and direction selectivity: horizontal input profiles in the spatial domain (left), where excitatory input (EX) is skewed toward the preferred direction (arrow) of the postsynaptic neuron and inhibitory input (IN) is symmetric. In the time domain, when the stimulus moves in the preferred direction (middle), this asymmetry leads to a fast rise in excitation such that before inhibition takes effect with a delay the spike threshold is passed (EX-IN, middle bottom). In contrast, when the stimulus moves in the null direction (right), excitation rises more slowly and is efficiently counterbalanced by delayed inhibition, such that the spike threshold is not reached.

Microcircuit of functionally characterized L2/3 PCs

A previous study using a similar LSPS approach reported that on average, the local sources of excitation and inhibition spatially overlap in a balanced manner across L2/3, L4, and L5 in V1.[19] However, this study did not conduct prior functional *in vivo* characterization of cells and determined excitation and inhibition in separate experiments. We further investigated this by comparing excitation and inhibition in the same cells: Although excitation and inhibition indeed largely overlapped on average, the difference between their horizontal distributions displayed an inverted "Mexican hat profile" that was recently also observed in anatomical data[23] but that was not reported in the study of Xu et al.[19]

To our knowledge, our study is the first to functionally map the local sources of excitation and inhibition for single *in vivo* characterized L2/3 PCs in V1. Functional connectivity is constrained by anatomical connectivity and additionally shaped by synaptic strength. As expected, the spatial organization of functional input maps in our study largely follows previously described anatomical connectivity.[23,46] Inhibition dominates within L2/3, while excitation dominates in L4 and L5. The overall horizontal extent of presynaptic input sources is ~300–400 μm. On average, in L2/3 the horizontal extents of excitation and inhibition are matched, whereas in L4 the horizontal extent of excitation exceeds that of inhibition (but see Holmgren et al.[47]). The functional input maps differ from the anatomy in the amount of functional excitatory input arising from L4, being on average lower than from L2/3, which is different to the relative numbers of presynaptic neurons located in L2/3 and L4.[46] This points to discrepancies in synaptic strength between different connections. Indeed, synaptic L4 → L2/3 connections are only about half as strong as L2/3 → L2/3 connections.[48] Even within the same cortical connection type, synapse strength was shown to vary over orders of magnitude, particularly in connections between L2/3 PCs in the mouse visual cortex.[20] Systematic variation of synaptic strength over the spatial distribution of presynaptic L2/3 PCs might be one factor underlying the skew we find in the excitatory input maps of direction-tuned L2/3 PCs, which has not been reported for the anatomical data[23] (see below). This highlights the importance of functional input mapping for circuit analysis, as it provides additional information beyond the anatomical arrangement of presynaptic neurons.

Relationship of intralaminar and interlaminar circuits to orientation tuning of L2/3 PCs

How intracortical excitatory and inhibitory circuits in L2/3 contribute to the generation of orientation tuning is still debated.[1,2] Regarding excitation, it has been demonstrated that the receptive fields of excitatory neurons presynaptic to L2/3 PCs tend to be co-oriented and aligned in visual space to the axis of the postsynaptic L2/3 PC's preferred orientation.[21–23,36] In our study, we found that the spatial distributions of presynaptic excitatory cells showed a tendency toward elongation along the cortical axis of preferred orientation (data not shown). The absence of a more pronounced elongation could be due to the lack of precise one-to-one mapping between the arrangement of presynaptic neurons in cortical space and the arrangement of the corresponding receptive fields in visual space, as has been previously described.[23]

We did not find evidence for overall differences in the laminar and horizontal excitatory and inhibitory input organization for highly orientation-selective cells versus untuned cells. It has been proposed that the relative horizontal organization of excitation and inhibition in the shape of an inverse Mexican hat profile might be responsible for sharpening orientation tuning in the visual cortex of species with a pinwheel-like organization of preferred orientations.[32] Since we did not find differences in the horizontal profiles between orientation-tuned and orientation-untuned cells, our data did not support such function for the inverse Mexican hat arrangement in mice. Although overall inhibition appears not distinctive for selective versus untuned L2/3 PCs, differences might be present at the level of interneuron subtypes. PV and SST interneurons seem to contribute to orientation selectivity in diverse ways, but their exact roles remain conflicting.[49–51] Given that glutamate uncaging unselectively activates neurons, we were not able to observe potential interneuron type specific effects.

Relationship of intralaminar and interlaminar circuits to direction tuning of L2/3 PCs

The circuit mechanisms leading to the emergence of direction tuning in L2/3 PCs across animal species are still under debate.[1,2] In ferret visual cortex, long-range intracortical inhibitory connections to L2/3 PCs have been shown to sharpen direction selectivity by suppressing responses to the null direction of motion.[52] In mouse visual cortex, L2/3 PCs could directly inherit direction selectivity from direction-selective ganglion cells via the shell region of the dLGN[42] or by sampling thalamocortical inputs with spatiotemporal offsets similar to L4 PCs.[53] Finally, the spatial offset between excitatory and inhibitory presynaptic ensembles in the reference frame of visual space has been proposed to contribute to direction selectivity in L2/3 PCs.[23]

In our study, we find that the distribution of presynaptic partners in cortical space was shifted opposite to the direction corresponding to the preferred direction of L2/3 PCs in visual space, both for excitation and inhibition. This is complementary to anatomical data obtained by monosynaptic rabies tracing, where the distribution of excitatory presynaptic cells was located opposite to each postsynaptic cell's preferred direction. In contrast, for inhibitory input, the anatomical data show an offset along and not opposite to the preferred direction.[23] The likely reasons for this apparent discrepancy are the difference in reference frames—cortical versus visual space—and differences between anatomical and functional connectivity as discussed above. Indeed, for the anatomical cell distributions in cortical space, offsets were not reported.[23] Interestingly, we found that although both excitation and inhibition are spatially offset to the same side, inhibition is symmetric around its mean, in contrast to excitation that was asymmetric. This strongly resembles observations from previous studies in L4 of mouse V1.[24,25] In their studies, Li et al. mapped the response amplitude of L4 PCs across their receptive field for both excitation and inhibition by *in vivo* patch-clamp recordings and systematically flashing a bar at different locations of the receptive field. Similar to our observation, Li et al. found that the distribution of input strength across the excitatory receptive field is spatially skewed toward the preferred direction of a cell, whereas the distribution in the inhibitory receptive field is more or less spatially symmetric.[24,25] Such spatial asymmetry in excitation translates into temporal asymmetries and can thereby contribute to direction selectivity: Excitation rises faster for movement in the preferred and slower in the null direction, such that inhibition, starting with a delay,[54] less effectively suppresses the excitatory response to the preferred direction compared with the null direction. Thereby, the spatial asymmetry in excitation could support reaching the spike threshold for stimuli in the preferred direction in contrast to the null direction (Figure 5B).

Taken together, we find that both the dendritic architecture and the spatial organization of the cortical microcircuit of L2/3 PCs are related to characteristic properties of neurons in the visual cortex: Orientation tuning is linked to apical dendritic complexity and elongation. Direction tuning is related to offsets and asymmetries in the spatial distribution of excitatory and inhibitory presynaptic partners. Our findings strongly suggest that the biased sampling of visual space that gives rise to visual tuning properties of L2/3 PCs is supported by their biased sampling of the cortical neighborhood as a result of asymmetries both at the level of dendritic morphology and the spatial organization of the functional microcircuit.

STAR★METHODS

Detailed methods are provided in the online version of this paper and include the following:

- KEY RESOURCES TABLE
- RESOURCE AVAILABILITY
  - Lead contact
  - Materials availability
  - Data and code availability
- EXPERIMENTAL MODEL AND SUBJECT DETAILS
  - Animals
- METHOD DETAILS
  - Virus preparation and dilution
  - Solutions
  - Virus injection and chronic window preparation
  - Intrinsic optical signal imaging
  - *In vivo* 2-photon imaging
  - Visual stimulation
  - Acute brain slice preparation and re-identification of cells
  - Laser Scanning Photostimulation (LSPS)
  - Image acquisition for morphological imaging
  - Immunohistochemistry
  - *In vivo* imaging analysis
  - Input map analysis
  - Morphological reconstruction and analysis
  - Estimation of the representation of stimulus orientation and direction in cortical space
  - Tuning curve sampling analysis
- QUANTIFICATION AND STATISTICAL ANALYSIS

SUPPLEMENTAL INFORMATION

Supplemental information can be found online at https://doi.org/10.1016/j.cub.2022.02.048.

ACKNOWLEDGMENTS

We are grateful to Volker Staiger for cell tracing as well as technical support, to Michael Myoga for helping to build the *in vitro* setups, to Pieter Goltstein for software, and to Alexander Borst for his comments on the manuscript. This study was supported by the Max Planck Society and the German Research Foundation (DFG, the Collaborative Research Center SFB870_A08, reference number 118803580 to V.S. and M.H.).

AUTHOR CONTRIBUTIONS

S.W. and V.S. conceived the project, with input from M.H., T.R., and T.B.; S.W. planned and performed all experiments; D.G.N. and S.W. wrote advanced analysis tools; D.G.N., S.W., T.R., and V.S. analyzed the data; S.W. and V.S. implemented LSPS at the patch-clamp setups; T.R. designed and built the *in vivo* two-photon setup and developed the viral construct; S.W., D.G.N., V.S., T.R., M.H., and T.B. wrote the manuscript; and T.B. provided the research environment.

DECLARATION OF INTERESTS

The authors declare no competing interests.

Received: August 12, 2021
Revised: December 6, 2021
Accepted: February 15, 2022
Published: March 10, 2022

REFERENCES

1. Niell, C.M., and Scanziani, M. (2021). How cortical circuits implement cortical computations: mouse visual cortex as a model. Annu. Rev. Neurosci. *44*, 517–546.
2. Priebe, N.J. (2016). Mechanisms of orientation selectivity in the primary visual cortex. Annu. Rev. Vis. Sci. *2*, 85–107.
3. Hubel, D.H., and Wiesel, T.N. (1962). Receptive fields, binocular interaction and functional architecture in the cat's visual cortex. J. Physiol. *160*, 106–154.
4. Garrett, M.E., Nauhaus, I., Marshel, J.H., and Callaway, E.M. (2014). Topography and areal organization of mouse visual cortex. J. Neurosci. *34*, 12587–12600.
5. Bonin, V., Histed, M.H., Yurgenson, S., and Reid, R.C. (2011). Local diversity and fine-scale organization of receptive fields in mouse visual cortex. J. Neurosci. *31*, 18506–18521.
6. Dräger, U.C. (1975). Receptive fields of single cells and topography in mouse visual cortex. J. Comp. Neurol. *160*, 269–290.
7. Shepherd, G.M.G., Stepanyants, A., Bureau, I., Chklovskii, D., and Svoboda, K. (2005). Geometric and functional organization of cortical circuits. Nat. Neurosci. *8*, 782–790.
8. Gouwens, N.W., Sorensen, S.A., Berg, J., Lee, C., Jarsky, T., Ting, J., Sunkin, S.M., Feng, D., Anastassiou, C.A., Barkan, E., et al. (2019). Classification of electrophysiological and morphological neuron types in the mouse visual cortex. Nat. Neurosci. *22*, 1182–1195.
9. Colonnier, M. (1964). The tangential organization of the visual cortex. J. Anat. *98*, 327–344.
10. Livingstone, M.S. (1998). Mechanisms of direction selectivity in macaque V1. Neuron *20*, 509–526.
11. Hübener, M., and Bolz, J. (1992). Relationships between dendritic morphology and cytochrome oxidase compartments in monkey striate cortex. J. Comp. Neurol. *324*, 67–80.
12. Anderson, J.C., Binzegger, T., Kahana, O., Martin, K.A.C., and Segev, I. (1999). Dendritic asymmetry cannot account for directional responses of neurons in visual cortex. Nat. Neurosci. *2*, 820–824.
13. Ohki, K., Chung, S., Ch'ng, Y.H., Kara, P., and Reid, R.C. (2005). Functional imaging with cellular resolution reveals precise micro-architecture in visual cortex. Nature *433*, 597–603.
14. Smith, S.L., Smith, I.T., Branco, T., and Häusser, M. (2013). Dendritic spikes enhance stimulus selectivity in cortical neurons in vivo. Nature *503*, 115–120.
15. Wang, C., Waleszczyk, W.J., Burke, W., and Dreher, B. (2007). Feedback signals from cat's area 21a enhance orientation selectivity of area 17 neurons. Exp. Brain Res. *182*, 479–490.
16. Park, J., Papoutsi, A., Ash, R.T., Marin, M.A., Poirazi, P., and Smirnakis, S.M. (2019). Contribution of apical and basal dendrites to orientation encoding in mouse V1 L2/3 pyramidal neurons. Nat. Commun. *10*, 5372.
17. Harris, K.D., and Mrsic-Flogel, T.D. (2013). Cortical connectivity and sensory coding. Nature *503*, 51–58.
18. Jiang, X., Shen, S., Cadwell, C.R., Berens, P., Sinz, F., Ecker, A.S., Patel, S., and Tolias, A.S. (2015). Principles of connectivity among morphologically defined cell types in adult neocortex. Science *350*, aac9462.
19. Xu, X., Olivas, N.D., Ikrar, T., Peng, T., Holmes, T.C., Nie, Q., and Shi, Y. (2016). Primary visual cortex shows laminar-specific and balanced circuit organization of excitatory and inhibitory synaptic connectivity. J. Physiol. *594*, 1891–1910.
20. Cossell, L., Iacaruso, M.F., Muir, D.R., Houlton, R., Sader, E.N., Ko, H., Hofer, S.B., and Mrsic-Flogel, T.D. (2015). Functional organization of excitatory synaptic strength in primary visual cortex. Nature *518*, 399–403.
21. Schwarz, C., and Bolz, J. (1991). Functional specificity of a long-range horizontal connection in cat visual cortex: a cross-correlation study. J. Neurosci. *11*, 2995–3007.
22. Iacaruso, M.F., Gasler, I.T., and Hofer, S.B. (2017). Synaptic organization of visual space in primary visual cortex. Nature *547*, 449–452.
23. Rossi, L.F., Harris, K.D., and Carandini, M. (2020). Spatial connectivity matches direction selectivity in visual cortex. Nature *588*, 648–652.
24. Li, Y.T., Liu, B.H., Chou, X.L., Zhang, L.I., and Tao, H.W. (2015). Strengthening of direction selectivity by broadly tuned and spatiotemporally slightly offset inhibition in mouse visual cortex. Cereb. Cortex *25*, 2466–2477.
25. Li, Y.T., Fang, Q., Zhang, L.I., and Tao, H.W. (2018). Spatial asymmetry and short-term suppression underlie direction selectivity of synaptic excitation in the mouse visual cortex. Cereb. Cortex *28*, 2059–2070.
26. Weiler, S., Bauer, J., Hübener, M., Bonhoeffer, T., Rose, T., and Scheuss, V. (2018). High-yield *in vitro* recordings from neurons functionally characterized *in vivo*. Nat. Protoc. *13*, 1275–1293.
27. Callaway, E.M., and Katz, L.C. (1993). Photostimulation using caged glutamate reveals functional circuitry in living brain slices. Proc. Natl. Acad. Sci. USA. *90*, 7661–7665.
28. Dantzker, J.L., and Callaway, E.M. (2000). Laminar sources of synaptic input to cortical inhibitory interneurons and pyramidal neurons. Nat. Neurosci. *3*, 701–707.
29. Marques, T., Nguyen, J., Fioreze, G., and Petreanu, L. (2018). The functional organization of cortical feedback inputs to primary visual cortex. Nat. Neurosci. *21*, 757–764.
30. Waters, J., Lee, E., Gaudreault, N., Griffin, F., Lecoq, J., Slaughterbeck, C., Sullivan, D., Farrell, C., Perkins, J., Reid, D., et al. (2019). Biological variation in the sizes, shapes and locations of visual cortical areas in the mouse. PLoS One *14*, e0213924.
31. Freund, T.F., and Katona, I. (2007). Perisomatic inhibition. Neuron *56*, 33–42.
32. Kang, K., Shelley, M., and Sompolinsky, H. (2003). Mexican hats and pinwheels in visual cortex. Proc. Natl. Acad. Sci. USA. *100*, 2848–2853.
33. Vélez-Fort, M., Rousseau, C.V., Niedworok, C.J., Wickersham, I.R., Rancz, E.A., Brown, A.P.Y., Strom, M., and Margrie, T.W. (2014). The stimulus selectivity and connectivity of layer six principal cells reveals cortical microcircuits underlying visual processing. Neuron *83*, 1431–1443.
34. Kim, E.J., Juavinett, A.L., Kyubwa, E.M., Jacobs, M.W., and Callaway, E.M. (2015). Three types of cortical layer 5 neurons that differ in brain-wide connectivity and function. Neuron *88*, 1253–1267.
35. Martin, K.A., and Whitteridge, D. (1984). Form, function and intracortical projections of spiny neurones in the striate visual cortex of the cat. J. Physiol. *353*, 463–504.
36. Bosking, W.H., Zhang, Y., Schofield, B., and Fitzpatrick, D. (1997). Orientation selectivity and the arrangement of horizontal connections in tree shrew striate cortex. J. Neurosci. *17*, 2112–2127.
37. Ji, W., Gămănuţ, R., Bista, P., D'Souza, R.D., Wang, Q., and Burkhalter, A. (2015). Modularity in the organization of mouse primary visual cortex. Neuron *87*, 632–643.
38. Roth, M.M., Dahmen, J.C., Muir, D.R., Imhof, F., Martini, F.J., and Hofer, S.B. (2016). Thalamic nuclei convey diverse contextual information to layer 1 of visual cortex. Nat. Neurosci. *19*, 299–307.
39. Jaepel, J., Hübener, M., Bonhoeffer, T., and Rose, T. (2017). Lateral geniculate neurons projecting to primary visual cortex show ocular dominance plasticity in adult mice. Nat. Neurosci. *20*, 1708–1714.
40. Andermann, M.L., Kerlin, A.M., Roumis, D.K., Glickfeld, L.L., and Reid, R.C. (2011). Functional specialization of mouse higher visual cortical areas. Neuron *72*, 1025–1039.
41. Marshel, J.H., Garrett, M.E., Nauhaus, I., and Callaway, E.M. (2011). Functional specialization of seven mouse visual cortical areas. Neuron *72*, 1040–1054.
42. Cruz-Martín, A., El-Danaf, R.N., Osakada, F., Sriram, B., Dhande, O.S., Nguyen, P.L., Callaway, E.M., Ghosh, A., and Huberman, A.D. (2014). A dedicated circuit links direction-selective retinal ganglion cells to the primary visual cortex. Nature *507*, 358–361.

43. Feldmeyer, D., Lübke, J., Silver, R.A., and Sakmann, B. (2002). Synaptic connections between layer 4 spiny neurone-layer 2/3 pyramidal cell pairs in juvenile rat barrel cortex: physiology and anatomy of interlaminar signalling within a cortical column. J. Physiol. *538*, 803–822.

44. Feldmeyer, D., Lübke, J., and Sakmann, B. (2006). Efficacy and connectivity of intracolumnar pairs of layer 2/3 pyramidal cells in the barrel cortex of juvenile rats. J. Physiol. *575*, 583–602.

45. Sun, W., Tan, Z., Mensh, B.D., and Ji, N. (2016). Thalamus provides layer 4 of primary visual cortex with orientation- and direction-tuned inputs. Nat. Neurosci. *19*, 308–315.

46. Wertz, A., Trenholm, S., Yonehara, K., Hillier, D., Raics, Z., Leinweber, M., Szalay, G., Ghanem, A., Keller, G., Rózsa, B., et al. (2015). Single-cell-initiated monosynaptic tracing reveals layer-specific cortical network modules. Science *349*, 70–74.

47. Holmgren, C., Harkany, T., Svennenfors, B., and Zilberter, Y. (2003). Pyramidal cell communication within local networks in layer 2/3 of rat neocortex. J. Physiol. *551*, 139–153.

48. Morgenstern, N.A., Bourg, J., and Petreanu, L. (2016). Multilaminar networks of cortical neurons integrate common inputs from sensory thalamus. Nat. Neurosci. *19*, 1034–1040.

49. Atallah, B.V., Bruns, W., Carandini, M., and Scanziani, M. (2012). Parvalbumin-expressing interneurons linearly transform cortical responses to visual stimuli. Neuron *73*, 159–170.

50. Lee, S.H., Kwan, A.C., Zhang, S., Phoumthipphavong, V., Flannery, J.G., Masmanidis, S.C., Taniguchi, H., Huang, Z.J., Zhang, F., Boyden, E.S., et al. (2012). Activation of specific interneurons improves V1 feature selectivity and visual perception. Nature *488*, 379–383.

51. Song, Y.H., Hwang, Y.S., Kim, K., Lee, H.R., Kim, J.H., Maclachlan, C., Dubois, A., Jung, M.W., Petersen, C.C.H., Knott, G., et al. (2020). Somatostatin enhances visual processing and perception by suppressing excitatory inputs to parvalbumin-positive interneurons in V1. Sci. Adv. *6*, eaaz0517.

52. Wilson, D.E., Scholl, B., and Fitzpatrick, D. (2018). Differential tuning of excitation and inhibition shapes direction selectivity in ferret visual cortex. Nature *560*, 97–101.

53. Lien, A.D., and Scanziani, M. (2018). Cortical direction selectivity emerges at convergence of thalamic synapses. Nature *558*, 80–86.

54. Haider, B., Häusser, M., and Carandini, M. (2013). Inhibition dominates sensory responses in the awake cortex. Nature *493*, 97–100.

55. Brainard, D.H. (1997). The psychophysics toolbox. Spat. Vis. *10*, 433–436.

56. Pologruto, T.A., Sabatini, B.L., and Svoboda, K. (2003). ScanImage: flexible software for operating laser scanning microscopes. Biomed. Eng. OnLine *2*, 13.

57. Schindelin, J., Arganda-Carreras, I., Frise, E., Kaynig, V., Longair, M., Pietzsch, T., Preibisch, S., Rueden, C., Saalfeld, S., Schmid, B., et al. (2012). Fiji: an open-source platform for biological-image analysis. Nat. Methods *9*, 676–682.

58. Cuntz, H., Forstner, F., Borst, A., and Häusser, M. (2011). The TREES toolbox–probing the basis of axonal and dendritic branching. Neuroinformatics *9*, 91–96.

59. Berens, P. (2009). CircStat: a MATLAB toolbox for circular statistics. J. Stat. Soft. *31*, 1–21.

60. Rose, T., Jaepel, J., Hübener, M., and Bonhoeffer, T. (2016). Cell-specific restoration of stimulus preference after monocular deprivation in the visual cortex. Science *352*, 1319–1322.

61. Leinweber, M., Zmarz, P., Buchmann, P., Argast, P., Hübener, M., Bonhoeffer, T., and Keller, G.B. (2014). Two-photon calcium imaging in mice navigating a virtual reality environment. J. Vis. Exp. *84*, e50885.

62. Suter, B.A., O'Connor, T., Iyer, V., Petreanu, L.T., Hooks, B.M., Kiritani, T., Svoboda, K., and Shepherd, G.M.G. (2010). Ephus: multipurpose data acquisition software for neuroscience experiments. Front. Neural Circuits *4*, 100.

63. Shepherd, G.M.G., and Svoboda, K. (2005). Laminar and columnar organization of ascending excitatory projections to layer 2/3 pyramidal neurons in rat barrel cortex. J. Neurosci. *25*, 5670–5679.

64. Kerlin, A.M., Andermann, M.L., Berezovskii, V.K., and Reid, R.C. (2010). Broadly tuned response properties of diverse inhibitory neuron subtypes in mouse visual cortex. Neuron *67*, 858–871.

65. Mazurek, M., Kager, M., and Van Hooser, S.D. (2014). Robust quantification of orientation selectivity and direction selectivity. Front. Neural Circuits *8*, 92.

66. Carandini, M., and Ferster, D. (2000). Membrane potential and firing rate in cat primary visual cortex. J. Neurosci. *20*, 470–484.

67. Stringer, C., Pachitariu, M., Steinmetz, N., Carandini, M., and Harris, K.D. (2019). High-dimensional geometry of population responses in visual cortex. Nature *571*, 361–365.

STAR★METHODS

KEY RESOURCES TABLE

REAGENT or RESOURCE	SOURCE	IDENTIFIER
Antibodies		
Monoclonal IgG rat anti-Ctip2	Abcam	RRID: AB_2064130
Rabbit anti-Calbindin D28k	Swant	Cat# CB-38a
Polyclonal IgG goat anti-rat Cy3	Jackson ImmunoResearch Labs	RRID: AB_2338244
Polyclonal IgG goat anti-Rabbit-Alexa-488	Thermo Fisher	Cat# A-11034
Bacterial and virus strains		
AAV2/1-Syn-FLEX-mRuby2-CSG-P2A-GCaMP6m-WPRE-SV40	Addgene	Cat# 51473
AAV2/1.CamKII0.4.Cre.SV40	University of Pennsylvania Vector Core	Cat# AV-1-PV2396
Chemicals, peptides, and recombinant proteins		
MNI-caged-L-glutamate	Tocris	Cat# 1490
Experimental models: Organisms/strains		
C57BL/6 mouse line	Local colony	N/A
Software and algorithms		
MATLAB, R2017/2018b	Mathworks	https://www.mathworks.com/products/matlab.html; RRID: SCR_001622
PsychToolbox	Brainard et al.[55]	http://psychtoolbox.org/download
ScanImage, v4.2	Pologruto et al.[56]; Vidrio Technologies	http://scanimage.vidriotechnologies.com/
LabView	National Instruments	https://www.ni.com/en-gb/shop/labview.html
Ephus	Vidrio Technologies	http://scanimage.vidriotechnologies.com/pages/viewpage.action?pageId=361641
ImageJ	Schindelin et al.[57]	RRID: SCR_002285
TREES toolbox	Cuntz et al.[58]	https://github.com/cuntzlab/treestoolbox
Custom code	This paper	https://github.com/drguggiana/Weiler_Guggiana_2022
circ_stats Toolbox	Behrens[59]	https://github.com/circstat/circstat-matlab
Other		
Explorer One 355-1 laser	Newport Spectra-Physics	https://www.spectra-physics.com/f/explorer-one-compact-laser
3500 DPSS laser	DPSS laser	https://www.dpss-lasers.com/series-3500-uv-laser-system
Miner's lamp with light source	BLS Biological Laboratory Equipment	cat. no. FHS/T01
Emission filter for miner's lamp 525–555 nm	BLS Biological Laboratory Equipment	cat. no. FS/ULS-02G
Emission filter for miner's lamp 590–660 nm	BLS Biological Laboratory Equipment	cat. no. FS/TEF-4R2

RESOURCE AVAILABILITY

Lead contact

Further information and requests for resources and reagents should be directed to and will be fulfilled by the lead contact, Volker Scheuss (Volker.Scheuss@med.uni-muenchen.de).

Materials availability

This study did not generate new unique reagents.

Data and code availability

Original data have been deposited to Mendeley Data at https://dx.doi.org/10.17632/p8n5m9h54g.1 and the code generated is available on Github at https://github.com/drguggiana/Weiler_Guggiana_2022.

EXPERIMENTAL MODEL AND SUBJECT DETAILS

Animals

All experimental procedures were carried out in compliance with institutional guidelines of the Max Planck Society and the local government (Regierung von Oberbayern). Experiments were performed on wild type C57bl/6 female mice (postnatal days P27-P70) housed under a 12 h light-dark cycle with food and water available ad libitum. Animals were usually group housed. After cranial window and head plate implantation animals were singly housed. All experiments were performed during the dark cycle of the animals.

METHOD DETAILS

Virus preparation and dilution

To co-express the genetically encoded calcium indicator GCaMP6m together with the structural marker mRuby2[60] in a sparse subset of L2/3 neurons the adeno-associated virus AAV2/1-Syn-FLEX-mRuby2-CSG-P2A-GCaMP6m-WPRE-SV40 (final titer: 1.4 x 10^{13} GC per ml, Addgene plasmid # 51473, dilution with PBS) was mixed with AAV2/1.CamKII0.4.Cre.SV40 (final titer: 3 x 10^{9}–4.5 x 10^{9}GC per ml, University of Pennsylvania Vector Core accession no. AV-1-PV2396[26]). This yielded labeling of ~10–20% of excitatory cortical cells.

Solutions

Cortex buffer for *in vivo* surgeries and imaging contained 125 mM NaCl, 5 mM KCl, 10 mM glucose, 10 mM HEPES, 2 mM $CaCl_2$ and 2 mM $MgSO_4$. The buffer was sterilized and maintained at pH 7.4.

The cutting solution for *in vitro* experiments contained 85 mM NaCl, 75 mM sucrose, 2.5 KCl, 24 mM glucose, 1.25 mM NaH_2PO_4, 4 mM $MgCl_2$, 0.5 mM $CaCl_2$ and 24 mM $NaHCO_3$ (310-325 mOsm, bubbled with 95% (vol/vol) O_2, 5% (vol/vol) CO_2). Artificial cerebrospinal fluid (ACSF) contained 127 mM NaCl, 2.5 mM KCl, 26 mM $NaHCO_3$, 2 mM $CaCl_2$, 2 mM $MgCl_2$, 1.25 mM NaH_2PO_4 and 10 mM glucose (305-315 mOsm, bubbled with 95% (vol/vol) O_2, 5% (vol/vol) CO_2). Caesium-based internal solution contained 122 mM $CsMeSO_4$, 4 mM $MgCl_2$, 10 mM HEPES, 4 mM Na-ATP, 0.4 mM Na-GTP, 3 mM Na-L-ascorbate, 10 mM Na-phosphocreatine, 0.2 mM EGTA, 5 mM QX-314, and 0.03 mM Alexa 594 (pH 7.25, 295-300 mOsm). K-based internal solution contained 126 mM K-gluconate, 4 mM KCl, 10 mM HEPES, 4 mM Mg-ATP, 0.3 mM Na-GTP, 10 mM Na-phosphocreatine, 0.3-0.5% (wt/vol) Neurobiotin tracer and 0.03 mM Alexa 594 (pH 7.25, 295-300 mOsm).

Virus injection and chronic window preparation

The detailed procedure is described elsewhere.[26] Briefly, surgeries were performed on 31 female C57bl/6 mice (postnatal days P27-P35) that were intraperitoneally (i.p.) anesthetized with a mixture of Fentanyl (0.05 mg kg^{-1}), Midazolam (5 mg kg^{-1}) and Medetomidine (0.5 mg kg^{-1}). Additional analgesic drugs applied were Carprofen (5 mg kg^{-1}, subcutaneous, s.c.) before surgery and Lidocaine (10%, topical to skin prior to incision). A section of skin over the right hemisphere starting from the dorsal scalp was removed and the underlying periosteum was carefully removed. A custom-machined aluminum head bar (oval shape, with an 8 mm opening and two screw notches) was carefully placed and angled over the binocular zone of the primary visual area. The precise location of the binocular zone was determined by intrinsic optical signal (IOS) imaging through the intact skull prior to the craniotomy in each animal (see section below). A circular craniotomy (4 mm diameter) centered over the binocular zone of the right primary visual cortex (bV1) was performed. The premixed virus was injected 200-500 μm below the pial surface at a single site in the binocular zone of V1 (50-100 nl/injection, ~ 10 nl/min ejected by pressure pulses at 0.2 Hz, using glass pipettes and a pressure micro injection system. Additionally, diluted fluorescent retrobeads (1:20 with cortex buffer, Lumafluor) were pressure injected (10-20 nl/injection, 5 nl/min) medial and lateral to the virus injection site at ~1500 μm from its center. The craniotomy was covered with a glass cover slip and was sealed flush with drops of histoacryl. The head bar and cover glass were then further stabilized by dental cement. After surgery, the animal was injected s.c. with saline (500 μl) and the anesthesia was antagonized by i.p. injection of Naloxone (1.2 mg kg^{-1}), Flumazenil (0.5 mg kg^{-1}) and Atipamezole (2.5 mg kg^{-1}). Carprofen (5 mg kg^{-1}, subcutaneous, s.c.) was administered the following two days. *In vivo* imaging was performed not earlier than 2 weeks after virus injection to allow for sufficient indicator expression.

Intrinsic optical signal imaging

For IOS imaging, the optical axis was orthogonal to the head bar. The brain surface was first illuminated with light of 530 nm to visualize the blood vessel pattern and subsequently with 735 nm for intrinsic imaging to localize bV1. Images were acquired using

a 4x air objective (NA 0.28, Olympus) and a CCD camera (12 bit, 250x348 pixel, 40 Hz). The camera was focused ~500 μm below the pial surface. Image acquisition and analysis software were custom written in MATLAB. The visual stimulus was a patch with a size of 20° x 40° displayed randomly to either the left or right eye at two distinct positions next to each other in the central visual field. Within the patch a sinusoidal grating was displayed in eight directions for 7 s (grating direction was changed every 0.6 s) with a temporal frequency of 2 cycles/s and a spatial frequency of 0.04 cycles/degree. Individual trials were separated by 8 s of a full-field gray stimulus (50% contrast). The entire stimulus sequence was applied at least 2 times for each eye and patch position during the surgery before virus injection and at least 3 times at the beginning of the first *in vivo* imaging session

In vivo 2-photon imaging

L2/3 PCs co-expressing GCaMP6m and the bright structural marker mRuby2 (mRuby2-CSG-P2A-GCaMP6m) were imaged *in vivo* using a tunable pulsed femtosecond Ti:Sapphire laser (Newport Spectra-Physics) and a customized commercial 2-photon microscope (16x 0.8 NA water immersion objective; B-Scope I, Thorlabs). The laser was tuned to λ=940 nm to simultaneously excite GCaMP6m and mRuby2. After rejecting excitation laser light (FF01-720/25, Semrock), the emitted photons passed through a primary beam splitter (FF560 dichroic, Semrock) and band pass filters (FF02-525/50 and FF01-607/70, Semrock) onto GaAsP photomultiplier tubes (H7422P-40, Hamamatsu) to separate green and red fluorescence.

Multiple imaging planes were acquired by rapidly moving the objective in the z-axis using a high-load piezo z-scanner (P-726, Physik Instrumente). The image volume for functional cellular imaging was 250 x 250 x 100 μm^3 with 4 inclined image planes, each separated by 25 μm in depth. Imaging frames of 512 x 512 pixels (pixel size 0.5 μm) were acquired at 30 Hz by bidirectional scanning of an 8 kHz resonant scanner while beam turnarounds were blanked with an electro-optic modulator (Pockels cell). Imaging was performed between 130-400 μm below the pial surface. Excitation power was scaled exponentially (exponential length constant ~150 μm) with depth to compensate for light scattering in tissue with increasing imaging depth. The average power for imaging was <50 mW, measured after the objective. The optical axis was adjusted orthogonal to the cranial window. ScanImage 4.2[56] and custom written hardware drivers were used to control the microscope.

After functional characterization of L2/3 PCs, at least two high-resolution structural image stacks with different field of view sizes were acquired at λ=940 nm/1040 nm. These stacks covered a volume from the pial surface down to L5/L6 containing the functionally characterized L2/3 pyramidal cells of interest and usually consisted of 1) 450 sections (512 x 512 pixels) with a pixel size of 0.5 μm collected in z-steps of 1.4 μm (imaged volume of 256 x 256 x 630 μm^3); 2) 350 sections (512 x 512 pixels) with a pixel size of 1.9 μm collected in z-steps of 2 μm (imaged volume of 972 x 972 x 700 μm^3).

Experiments were performed under light anesthesia. Data acquisition started ~45 min after an i.p. injection of Fentanyl (0.035 mg kg^{-1}), Midazolam (3.5 mg kg^{-1}) and Medetomidine (0.35 mg kg^{-1}). Additional doses of anesthetics (25% of induction level) were subcutaneously injected every 45–60 mins to maintain the level of anesthesia. Ophthalmic ointment was applied to protect the eyes. Mice were fixed under the microscope by screwing the metal head-plate to two posts. Stable thermal homeostasis was maintained by using a heated blanket throughout the imaging session. Eye and pupil positions were recorded with two cameras (DMK 22BUC03, The Imaging Source Europe GmbH) throughout *in vivo* imaging.

Visual stimulation

Visual stimuli were generated using the MATLAB Psychophysics Toolbox extension and displayed on a gamma-corrected LCD monitor, http://psychtoolbox.org[55]). The screen measured 24.9 x 44.3 cm, had a refresh rate of 60 Hz, and was positioned in portrait orientation 13 cm in front of the eyes of the mouse, providing a viewing angle of ~45° on each side from the center of the monitor. The monitor was adjusted in position (horizontal rotation and vertical tilt) for each mouse to align with the horizontal visual axis and cover the binocular visual field (-15° to 35° elevation and -25° to 25 azimuth relative to midline). The presented stimulus area was chosen to subtend binocular visual space. The rest of the screen was uniformly grey (50% contrast). An OpenGL shader was applied to all presented stimuli to correct for the increasing eccentricity on a flat screen relative to the spherical mouse visual space.[41] Randomly alternating monocular stimulation of the eyes was achieved by motorized eye shutters and custom MATLAB scripts.

For all visual stimuli presented, the backlight of the LED screen was synchronized to the resonant scanner, switching on only during the bidirectional scan turnaround periods when imaging data were not recorded.[61] The mean luminance with 16 kHz pulsed backlight was 0.01 cd/m^2 for black and 4.1 cd/m^2 for white.

To measure visually evoked responses, the right or left eye was visually stimulated in random order using drifting black and white square wave gratings of eight directions with a temporal frequency of 3 cycles/s and a spatial frequency of 0.04 cycles/degree. The definition of drifting grating orientation and direction angles is given in Figures 2C and 4A. Stimulation duration for moving gratings was 5 s interleaved by 6 s of a full-field grey screen. Trials were repeated 4 times per eye and direction.

Acute brain slice preparation and re-identification of cells

The detailed procedure is described elsewhere.[26] Briefly, naive mice (P27-P70) and mice one day after *in vivo* imaging were deeply anesthetized with Isoflurane in a sealed container (>100 mg/kg) and rapidly decapitated. Coronal sections of V1 (320 μm, Bregma -1.5 to -3) were cut in ice cold carbogenated cutting solution using a vibratome (VT1200S, Leica). Slices were incubated in cutting solution in a submerged chamber at 34°C for at least 45 min and then transferred to ACSF in a light-shielded submerged chamber at room temperature (21°C) until used for recordings. Brain slices were used for up to 6 hours after dissection. A single brain slice was mounted on a poly-D-lysine coated coverslip[26] and then transferred to the recording chamber of the *in vitro* 2-photon microscope

(A-scope, Thorlabs) while keeping track of the rostro-caudal orientation of the slice. The fluorescence bead deposits in the brain slice were used to locate the area of interest. Following this, a high-resolution image stack was acquired from the slice surface to the bottom using a 16x objective and a wavelength of 1040 nm to excite mRuby2. ScanImage 4.2 and custom written hardware drivers were used to operate the *in vitro* 2-photon microscope. The *in vitro* stack consisted of 200-320 sections (512 x 512 pixels; 0.5 - 2 μm pixel size) recorded in z steps of 1-2 μm. As a next step, the relative positions of cells and morphological details such as blood vessel patterns were compared between the side view of the *in vivo* stack and the face view of the *in vitro* stack. Z-projections of sections of the *in vivo* side view and *in vitro* stacks were created in ImageJ[57] and used to compare and match cell patterns in z-projections by eye. The reidentifed cells were recorded in the slice at random with respect to their *in vivo* response properties. The reidentified cells were 41-110 μm below the slice surface (average: 66.61 ± 2.07 μm, n = 70 cells). Deeper cells were not accessible for electrophysiological input mapping.

Laser Scanning Photostimulation (LSPS)

For uncaging experiments, coronal brain slices were visualized using infrared Dodt gradient contrast (DGC) with a low magnification UV transmissive objective (4x objective lens). Images were acquired by a high-resolution digital CCD camera. The MNI-caged-L-glutamate concentration was 0.2 mM. The bath solution was replaced after 3 h of recording, and bath evaporation was counterbalanced by adding constantly a small amount of distilled H_2O to the solution reservoir using a perfusor. 2-photon guided targeted patching was performed on cells that were matched *in vivo* and *in vitro*. Borosilicate glass patch pipettes (resistance of 4-5 MΩ) were filled with a Cs-based internal solution for measuring excitatory and inhibitory postsynaptic currents (EPSC: voltage clamp at -70 mV, IPSC: voltage clamp at 0-5 mV). Once stable whole-cell recordings were obtained (access resistance < 30 MΩ) the microscope objective was switched from 60x to 4x for circuit mapping. Mapping experiments were controlled with Ephus software,[62] The slice was positioned within the CCD camera's field of view and a stimulus grid (16 x 16 with 69 μm spacing) was aligned to the pial surface. Multiple maps were recorded with grid locations stimulated in a pseudo-random fashion (1 ms pulses, 10-15 mW in the specimen plane, 1s interstimulus interval, 2-3 repetitions each with different mapping sequence) for both excitatory and inhibitory inputs. The UV laser for glutamate uncaging was an Explorer One 355-1 (Newport Spectra-Physics). The duration and intensity of the laser pulses were controlled using the built-in software L-Win (Newport Spectra-Physics), a mechanical shutter as well as neutral density filters. The laser beam was scanned using voltage-controlled mirror galvanometers. An UV-sensitive photodiode measured the power of the UV laser beam. A dichroic mirror reflected the UV beam into the optical axis of the microscope while transmitting visible light for capturing bright-field images by the CCD camera. The beam passed a tube/scan lens pair in order to underfill the back aperture of the 4x mapping objective resulting in a pencil-shaped beam.

Data were acquired with a Multiclamp 700 B amplifier (Axon instruments). Voltage clamp recordings were filtered at 4-8 kHz and digitized at 10 kHz. Data Analysis was performed using custom-written software in MATLAB.

The spatial resolution of photostimulation was estimated by recording excitation profiles.[63] Excitation profiles describe the spatial resolution of uncaging sites that generate action potentials in stimulated neurons. For this, excitatory as well as inhibitory cells in different layers of bV1 were recorded either in whole-cell or cell-attached configuration using a K-based internal solution in current-clamp mode. Mapping was performed as described above only that the stimulus grid was 8x8 or 8x16 with 50 or 69 μm spacing. In a subset of these experiments, a second setup (setup B, microscope: BW51X, Olympus) equipped with a diode-pumped solid-state laser (DPSS laser) was used to generate 355 nm UV laser pulses for glutamate uncaging. The duration and intensity of the laser pulses were controlled by an electro-optical modulator, a neutral density filter wheel and a mechanical shutter.

Image acquisition for morphological imaging

The patch pipette was carefully retracted from the cell after successful recording and filling with Alexa-594. A detailed structural 2-photon image stack of the dendritic morphology of the entire cell was acquired with excitation light of λ=810 nm using ScanImage 4.2.[56] The structural image stacks typically consisted of 250 sections (1024 x 1024 pixels; 0.3-0.8 μm per pixel) collected in z steps of 1-2 μm. A second identical image stack was acquired at λ=940/1040 nm to visualize mRuby2. An overlay of the acquired stacks (in ImageJ) was then used to verify that the *in vivo* functionally characterized cell of interest was successfully re-identified, recorded, and filled with Alexa 594. The succesfully reconstructed cells were 45-110 μm below the slice surface (average: 68.53 ± 3.08 μm, n=36 cells).

Immunohistochemistry

For cortical layer analysis, animals were perfused transcardially with saline with an addition of Heparin (5mg/l)/Lidocain (2.8 mg/l) followed by 4% paraformaldehyde (PFA, wt/vol). Brains were dissected, post-fixed in 4% PFA for 24–72h, and placed in 30% sucrose (vol/vol) for 24–48 h. Brains were then cut on a freezing microtome to 50 μm sections and collected in PBS. After cutting, brain slices were washed in PBS and incubated in Na-Citrate buffer at 95°C following the Heat-Induced Epitope retrieval (HIER) protocol (https://www.abcam.com/protocols/ihc-antigen-retrieval-protocol). Following this, slices were incubated in 10% NGS / 1% Triton X-100 in PBS overnight at 4°C. Slices were then incubated in rat anti-Ctip2 (Abcam ab18465, 1:200) and rabbit anti-Calbindin D28k (CB-38a, Swant, 1:2500) in 5% NGS first for 4 h at room temperature and then 20 h at 4°C. All sections were washed 3×10 min in PBS and incubated in goat anti-rat Cy3 (112-165-044, Jackson Immuno Research, 1:200) and Goat Anti-Rabbit Alexa Fluor 488 (A-11034, Thermo Fisher, 1:200) in 5% NGS for 3 h at room temperature. All sections were then washed 3×10 min in PBS followed by DAPI staining (Cat. No. D3571, ThermoFisher 1:1000) in PBS for 10 min, and then washed 3 × 10 min in PBS and aqua dest before

mounting onto Superfrost slides and coverslipping with FluorSave Reagent (Cat. No. 345789, Merck-Calbiochem). The sections were imaged at 10x using an AxioImager microscope (Zeiss).

In vivo imaging analysis

Custom-written MATLAB code was used for image and data analysis.

For intrinsic optical signal imaging analysis, the acquired images were high-pass filtered and clipped (1.5%) to calculate blank-corrected image averages for each condition. Additionally, a threshold criterion (image background mean + 4 x standard deviation) was set to determine the responsive region within the averaged image. The mean background value of the non-responsive region was subtracted from each pixel and all pixel values within the responsive area were summed to obtain an integrated measure of response strength.

In the case of 2-photon calcium imaging, the use of GCaMP6m in combination with mRuby2 gave the possibility to perform ratiometric imaging.[60] Image sequences were full-frame corrected for tangential drift and small movements caused by heart beat and breathing. An average of 160 image frames acquired without laser excitation was subtracted from all frames of the individual recording to correct for PMT dark current as well as residual light from the stimulus screen. Cell body detection was based on the average morphological image derived from the structural channel (mRuby2) for each recording session. ROIs (region of interest) were drawn manually, annotated and re-identified in subsequent imaging sessions. The fluorescence time course was calculated by averaging all pixel values within the ROI on both background-corrected channels, followed by low-pass filtering (0.8 Hz cut-off) and by subtraction of the time-variable component of the neuropil signal (pixel average within a band of 15 μm width, 2 μm away from the ROI circumference, excluding overlap with other selected cells and neuropil bands, neuropil factor r of 0.7[64]). The green and red fluorescence signals were estimated as:

$$Fgreen_{cell}(t) = Fgreen_{cell\_measured}(t) - r \times Fgreen_{neuropil}(t) + r \times median(Fgreen_{neuropil}(t))$$

$$Fred_{cell}(t) = Fred_{cell\_measured}(t) - r \times Fred_{neuropil}(t) + r \times median(Fred_{neuropil}(t))$$

The ratio R(t) was then calculated as:

$$R(t) = \frac{Fgreen_{cell}(t)}{Fred_{cell}(t)}$$

Slow timescale changes were removed by subtracting the 8th percentile of a moving 14 s temporal window from R(t). $\Delta R/R_0$ was calculated as:

$$\Delta R / R_0 = \frac{R - R_0}{R_0}$$

where single-trial $R_{0,trial}$ was measured over a 1 s period preceding visual stimulation. The median of all $R_{0,trial}$ values was taken as aggregate R_0 and used for $\Delta R/R_0$ calculations. Visual responses were extracted as mean fluorescence ratio change over the full stimulus interval ($\Delta R/R_{stim}$), either from individual trials or the trial-averaged mean response.

To determine visual responsiveness, a one-way ANOVA was performed over all single-trial $\Delta R/R_{stim}$ and 'blank' $\Delta R/R_{0,trial}$ values per orientation and both eyes in the case of monocular stimulation, or only a single condition in the case of binocular stimulation. Neurons with p values < 0.05 were identified as visually responsive.

OD was determined by the OD index (ODI) for each individual cell:

$$ODI = \frac{\frac{\Delta R}{R_0} contra_{pref\_dir} - \frac{\Delta R}{R_0} ipsi_{pref\_dir}}{\frac{\Delta R}{R_0} contra_{pref\_dir} + \frac{\Delta R}{R_0} ipsi_{pref\_dir}}$$

Where an ODI value of 1 or -1 indicates exclusive contra- and ipsilateral dominance, respectively.

Global orientation selectivity index (gOSI) was computed as 1 - circular Variance (circ. Var.):

$$gOSI = 1 - circ.var. = \left| \frac{\sum R(\theta_k) e^{2i\theta_k}}{\sum R(\theta_k)} \right|$$

and global direction selectivity index (gDSI) was computed as:

$$gDSI = 1 - dir.circ.var. = \left| \frac{\sum R(\theta_k) e^{i\theta_k}}{\sum R(\theta_k)} \right|$$

$R(\theta_k)$ is here the mean response to the direction angle (θ_k).[65] Perfect orientation and direction selectivity is indicated with gOSI and gDSI of 1, whereas a gOSI and gDSI value of 0 indicates no orientation or direction selectivity, respectively. The preferred orientation and direction as well as tuning width were computed by fitting a double-Gaussian tuning curve to the responses as previously described.[66] The tuning width was extracted as the sigma of the fitted curve. The goodness-of-fit was assessed by calculating R^2 and only cells with R^2 >0.3 were included in the analysis.

For the comparison between cells with aligned and nonaligned direction preference (Figure 4), cells with direction preference within sectors of 80° around the directions of 106° (106°-24° to 106°+56°) and 286° (286°-56° to 233+24°; aligned) and of 53° 53°-56° to 53°+24°) and 233° (233°-24° to 233°+56°; nonaligned) were combined. The neuron's assignment to the respective sector was based on the preferred direction of the dominant eye (|ODI|>0.25). For cells with $|ODI| \leq 0.25$, we only included neurons for which both eye-specific preferred directions fell into the same orientation sector.

Input map analysis

The spatial resolution of LSPS by UV glutamate uncaging was calculated based on the size of the excitation profiles as the mean weighted distance from the soma (d_{soma}) of AP generating sites using the following equation:[63]

$$R = \frac{\sum APs \times d_{soma}}{\sum APs}$$

LSPS by UV glutamate uncaging induces two types of responses:[28,63] 1) Direct glutamate uncaging responses originating from activation of glutamate receptors of the recorded neuron by the uncaged glutamate itself. 2) Synaptic responses originating from activation of glutamate receptors on the recorded neuron by glutamate released from stimulated presynaptic neurons. Responses to the LSPS stimulation protocol (both for EPSCs and IPSCs) were quantified in the 150 ms window following the uncaging light-pulse, since this is the time window where evoked activity is normally observed. Considering the diversity of responses encountered in these experiments, a heuristic analysis scheme was devised to address the main observed cases:

1) Inactive traces were excluded by only considering those responses with a deflection higher than 2 S.D. over the baseline at any point. Additionally, traces that only had a significant response in one repetition were also excluded.
2) Then, purely synaptic responses, i.e., those that correspond only to activation of the presynaptic neuron via uncaged glutamate were selected by taking the traces that passed the 2 S.D. threshold only after a 7 ms window from the offset of stimulation.
3) For responses that did not pass the previous criterion, inspection by eye indicated that several of them presented all the identifiable features of purely synaptic responses but seemed to cross the threshold slightly earlier than 7 ms. An additional set of experiments performed on a subset of cells, where maps were measured before and after application of TTX (and hence before and after only direct responses were present) were performed to characterize these intermediate cases (~5% of the total number of traces). These experiments showed that by using a secondary window of 3.5 ms, the average contribution of a direct response to the overall response in these intermediate traces is ~20 % (data not shown). Therefore, this secondary window was used to include a second set of traces into the synaptic response pool.
4) Finally, those traces that did not pass the secondary window were then blanked, and a 4-dimensional interpolation method (MATLAB function "griddatan") was used to infer their temporal profiles based on their 8 neighboring pixel activities in space and time. In the TTX experiments (data not shown) every position with a response was observed to have a synaptic component, but the summation of this synaptic component and the overlapping direct component is non-linear. Therefore, this interpolation method was used to extract the synaptic component partially masked in the raw traces by the direct response. The approach relies on the observation that the synaptic responses of neighboring positions are similar across time, therefore indicating that information on the synaptic responses masked by direct responses is contained in the responses surrounding them. These interpolated responses were then incorporated into the maps as synaptic responses. For excitatory input maps, the first two stimulation rows were excluded since L1 contains no excitatory neurons.[18] In some cases, apparent excitatory input from L1 originated from cells in L2/3-L5 having apical tuft dendrites in L1, which fired action potentials when their tufts were stimulated in L1 (see Figure S5).

To calculate the layer specific weighted centroid for each map, the weighted centroid was calculated according to the following formula:

$$(Centroid\ x,\ Centroid\ y) = \left(\frac{\sum x \times w}{\sum w}, \frac{\sum y \times w}{\sum w}\right)$$

Here x and y are the horizontal and vertical coordinates of every pixel assigned to the respective layer of interest (2/3, 4 or 5), and w is the input value associated with that position.

To calculate the slope of the spatial input distribution profiles, we first peak-normalized the input maps and computed the input fractions per column of the stimulation grid the respective layer of interest (2/3, 4 or 5). Then we used these fractional horizontal input profiles to calculate the slope between the 10 and 90 percentiles on the left and right side.

Morphological reconstruction and analysis

The reconstruction of dendritic cell morphology was performed manually using the Simple Neurite Tracer of ImageJ.[57] Reconstructions were quantitatively analyzed in MATLAB and with the open-source TREES toolbox.[58] The radial distance was measured as the Euclidean distance from the soma to each segment terminal. The total length was measured as the sum of all internode sections' length of the neurite. For Sholl analysis, the number of intersections between dendrites and concentric spheres

centered on the soma was determined at increasing distances from soma (20 μm increments). The distance to peak branching was measured as the distance of maximal dendritic branching from the soma. The width/height ratio was measured as the overall maximum horizontal extent divided by the overall maximum vertical extent.

Estimation of the representation of stimulus orientation and direction in cortical space

The retinotopic maps from 60 C57bl6 adult mice were downloaded from the Allen Brain Institute, as described in Waters et al.[30] These maps contain the elevation and azimuth as mapped across visual cortex using drifting bars in multiple directions (for details, refer to Waters et al.[30]). For each map, a 500x500 μm virtual section was positioned in the canonical position of the slices in this study (Figure S3A). The respective elevation and azimuth values were then obtained for all four edges of the slice (Figure S3B, left). These values were averaged and subsequently used to define the changes in elevation and azimuth of a stimulus corresponding to the medio-lateral axis, and likewise for a stimulus spanning the antero-posterior axis of the virtual section. The following equation was utilized for the mapping:

$$x = \tan(\theta)D \text{ and } y = \tan(\varphi)D$$

Where θ and φ are the average azimuth and elevation angles obtained from the retinotopic maps, at either the medial, lateral, anterior or posterior edge of the slice, D is the distance to the screen (10 cm as described in Waters et al.[30]) and x and y are the corresponding visual space coordinates (Figure S3B, right). These coordinates were then converted into stimulus angles in visual space using the following equation:

$$\psi = \arctan\left(\frac{y_2 - y_1}{x_2 - x_1}\right)$$

Where x_i and y_i are the horizontal and vertical visual space coordinates corresponding to either the M-L or A-P cortical locations, obtained from the elevation and azimuth maps (equation above), and ψ is the angle subtended by a line spanning the corresponding M-L or A-P edges of the slice in visual space. The angle values were finally rotated 90 degrees counterclockwise to convert them from the left hemisphere (where the maps were recorded) into the right (used in this study), and 0 was set towards the left of the screen, to match our stimulus display. This resulted in distributions of angles in visual space corresponding to the M-L and A-P axes of the coronal slices in our study from independent data in 60 animals (Figures S3C and S3D).

To simulate potential variation in slicing angle, the elevation and azimuth values were obtained for virtual slices artificially rotated by -10, -5, 5 and 10 degrees, followed by the same calculations described above. We found that slicing angle imprecisions within ±10° causes virtually no more variation (Figures S3E and S3F) than that arising from inter animal variability (Figures S3C and S3D).

Tuning curve sampling analysis

To account for the use of only eight sampling directions in the determination of tuning curves in this study, data from a different study with higher direction sampling coverage were taken. In particular, in Stringer et al.,[67] the authors record calcium transients from mouse L2/3 V1 cells while the animal is presented with 64 repetitions of gratings moving in 32 different directions. From this dataset, 300 cells were taken as the starting point for the analysis. The activity of the cells was averaged across trials, and the resulting tuning curves were fit with the algorithm described in Carandini and Ferster.[66] From the 300 cells, 130 passed the threshold of fit R2 (>0.3) used above. The resulting tuning curves were then undersampled by a factor of 4, using all four possible combinations of evenly spaced eight directions (Figure S4A). The tuning width of the reduced tuning curves was subtracted from the original tuning curve, and averages were calculated for each cell. This generated a distribution of delta tuning widths with a median of 10.96° (Figure S4B), which supports that we can resolve the tuning width to the degree shown in Figure 2G.

QUANTIFICATION AND STATISTICAL ANALYSIS

Data are reported as mean ± standard error of the mean (SEM). Correlation coefficients were calculated as Pearson's correlation coefficient. The Circular Statistics Toolbox developed by Philipp Berens was utilized for circular correlation calculation (https://www.mathworks.com/matlabcentral/fileexchange/10676-circular-statistics-toolbox-directional-statistics). Before comparison of data, individual data sets were checked for normality using the Kolmogorov-Smirnov Goodness-of-Fit test. None of the data sets considered in this study was found to be normally distributed. Therefore, paired or unpaired nonparametric statistics (Wilcoxon rank-sum test or signed-rank) were used for comparison. Two-tailed tests were used unless otherwise stated. Asterisks indicate significance values as follows: *$p < 0.05$, **$p < 0.01$, ***$p < 0.001$.